

Cite this: *Mater. Adv.*, 2025,  
6, 5546

# Dual-functional Tm<sup>3+</sup>/Yb<sup>3+</sup>-doped LiCaLa(MoO<sub>4</sub>)<sub>3</sub> phosphors: high-sensitivity thermal sensing and deep-tissue NIR bio-imaging

Ikhlas Kachou,<sup>a</sup> Kamel Saidi,<sup>ab</sup> Zein El Abidine Aly Taleb,<sup>a</sup>  
Christian Hernández-Álvarez,<sup>cd</sup> Mohamed Dammak<sup>ib</sup>\*<sup>a</sup> and  
Inocencio R. Martín<sup>ib</sup><sup>c</sup>

Thermal sensing and optical bio-imaging are critical in materials science for applications ranging from biomedical diagnostics to industrial monitoring. Herein, we report the first-time synthesis of a novel Mo-based host matrix, LiCaLa(MoO<sub>4</sub>)<sub>3</sub>, co-doped with Tm<sup>3+</sup>/Yb<sup>3+</sup>, specifically designed for upconversion luminescence with dual optical functionalities. These phosphors were engineered to exhibit red and near-infrared (NIR) emissions for dual-functional optical sensing and imaging. The temperature-dependent NIR fluorescence (650–1000 nm) was systematically investigated to evaluate their potential as thermal sensors within the first biological window (650–950 nm), which is essential for *in vivo* applications due to minimal tissue absorption. Using the fluorescence intensity ratio (FIR) method under 975 nm excitation, the phosphor demonstrated exceptional thermal sensitivity in two distinct regimes: (i) a high relative sensitivity of 2.62% K<sup>-1</sup> at 298 K from thermally coupled energy levels, enabling precise low-temperature detection with sub-degree resolution, and (ii) a robust relative sensitivity of 1.4% K<sup>-1</sup> at elevated temperatures (up to 748 K) from non-thermally coupled levels, suitable for high-temperature industrial sensing. Unlike previously reported host lattices, our LiCaLa(MoO<sub>4</sub>)<sub>3</sub> system integrates both temperature sensing and deep-tissue imaging capabilities into a single structure, offering a rare and efficient multifunctional solution. Furthermore, the material achieved tissue penetration depths of 4 mm, validating its dual utility for luminescence-based thermal sensing and deep-tissue bio-imaging. These findings not only highlight the unique properties of the LiCaLa(MoO<sub>4</sub>)<sub>3</sub> matrix but also establish it as a pioneering multifunctional platform in the field of NIR-based nanodiagnostics.

Received 14th May 2025,  
Accepted 1st July 2025

DOI: 10.1039/d5ma00489f

rsc.li/materials-advances

## Introduction

One of the most intensively studied phenomena in recent years is upconversion (UC) materials, which convert low-energy near-infrared (NIR) photons into higher-energy emissions. These materials are widely utilized in medicine for photodynamic therapy, cancer marker detection, bioimaging, and targeted drug delivery.<sup>1,2</sup> Among these, UC microparticles where sequential absorption of multiple photons generates

shorter-wavelength emissions have attracted significant research interest due to their unique optical properties.<sup>3–5</sup>

Remote temperature sensing has emerged as a key application of UC processes, as precise thermal monitoring is critical for understanding biological processes and disease management.<sup>6–8</sup> Lanthanide ions (Ln<sup>3+</sup>) are particularly promising for optical thermometry and biomedical applications due to their low toxicity, long luminescence lifetimes, photostability, and chemical robustness.<sup>9,10</sup> Yb<sup>3+</sup> ions, acting as sensitizers, efficiently absorb NIR light and transfer energy to activators (*e.g.*, Tm<sup>3+</sup>, Er<sup>3+</sup>, Ho<sup>3+</sup>) through stepwise processes, enabling emissions spanning ultraviolet (UV) to NIR ranges. Developing UC thermometers operating within the first biological window (IBW, 650–950 nm) where tissue absorption and scattering are minimal is critical for *in vivo* applications.<sup>11</sup>

Remote luminescent thermometers typically employ the fluorescence intensity ratio (FIR) method, which leverages thermally coupled levels (TCLs) in Ln<sup>3+</sup> ions. TCLs, defined by small energy gaps ( $200 \leq \Delta E \leq 2000 \text{ cm}^{-1}$ ), enable

<sup>a</sup> Laboratoire de Physique Appliquée, Faculté des Sciences de Sfax, Département de Physique, Université de Sfax, BP 1171, Sfax, Tunisia.

E-mail: madidammak@yahoo.fr, mohamed.dammak@fss.usf.tn

<sup>b</sup> Department of Physics, Sfax Preparatory Engineering Institute, University of Sfax, 1172-3000 Sfax, Tunisia

<sup>c</sup> Departamento de Física, MALTA-Consolider Team, Universidad de La Laguna, IMN and IUEA Apdo. Correos 456, E-38206, San Cristóbal de La Laguna, Santa Cruz de Tenerife, Spain

<sup>d</sup> Faculty of Chemistry, Adam Mickiewicz University, Uniwersytetu Poznańskiego 8, 61-614 Poznań, Poland



temperature-dependent shifts in emission intensity ratios *via* thermal population redistribution.<sup>12–14</sup> While Ho<sup>3+</sup> and Er<sup>3+</sup> emit in the visible range (green to orange), their utility is limited by shallow tissue penetration.<sup>9,15–17</sup> Conversely, Tm<sup>3+</sup> exhibits red (695 nm) and NIR (800 nm) emissions within the first biological window (IBW), offering superior penetration depths for deep tissue imaging.<sup>16</sup> However, TCL-based Tm<sup>3+</sup> sensors often show low sensitivity at high temperatures due to fixed energy gaps. Recent studies focus on non-thermally coupled levels (non-TCLs) of Ln<sup>3+</sup> ions, which provide tunable energy gaps for enhanced sensitivity.

Ratiometric luminescent thermometers using Tm<sup>3+</sup> are particularly advantageous due to their compatibility with the IBW, minimizing interference from water and hemoglobin.<sup>7–19</sup> These properties enable applications in cellular thermometry, cancer theranostics, and bioimaging.<sup>18–20</sup> Optical coherence tomography (OCT), initially developed for intracellular imaging, has expanded to visualize retinal structures<sup>17</sup> and now serves as a versatile tool for imaging skin, tumors, blood vessels, and other tissues.<sup>16</sup>

Among various host lattices, molybdate-based compounds have emerged as promising platforms for upconversion applications due to the favorable properties of MoO<sub>4</sub><sup>2–</sup> tetrahedra. These structural units introduce significant local asymmetry, which enhances the probability of forbidden 4f–4f transitions and boosts upconversion efficiency. Additionally, the presence of heavy Mo<sup>6+</sup> ions facilitates more effective phonon-assisted energy transfer while helping suppress non-radiative multiphonon relaxation owing to the relatively low phonon energy of the molybdate framework. These features enable Mo-based hosts to support intense red and NIR upconversion emissions, making them highly suitable for both thermal sensing and deep-tissue bioimaging.

In this work, we report the synthesis and investigation of LiCaLa(MoO<sub>4</sub>)<sub>3</sub> (LCLMO) microparticles doped with Yb<sup>3+</sup>/Tm<sup>3+</sup>, prepared *via* a high-temperature solid-state method. In addition, this host matrix exhibits high thermal and chemical stability, and the combination of alkali (Li<sup>+</sup>), alkaline earth (Ca<sup>2+</sup>), and lanthanide (La<sup>3+</sup>) cations allows tunable crystal field environments, which can further influence and optimize luminescent properties. These advantages make it a suitable and versatile platform for UC applications. We explore in detail the structural, upconversion (UC) emission, and photothermal properties of LCLMO:Tm<sup>3+</sup>/Yb<sup>3+</sup>. The results reveal a rare and valuable dual functionality: (1) high-sensitivity optical thermometry based on the fluorescence intensity ratio (FIR) of non-thermally coupled levels (non-TCLs), and (2) effective deep-tissue bioimaging within the first biological window (IBW). This unique combination of thermal and biomedical performance within a single crystalline host positions LCLMO:Tm<sup>3+</sup>/Yb<sup>3+</sup> as a pioneering multifunctional platform for next-generation optical diagnostics and non-invasive sensing technologies.

## Synthesis of LCLMO doped Tm<sup>3+</sup>/Yb<sup>3+</sup>

In this study, Tm<sup>3+</sup>/Yb<sup>3+</sup>-doped LCLMO phosphors were synthesized *via* a solid-state reaction method. The precursor materials

Li<sub>2</sub>CO<sub>3</sub>, La<sub>2</sub>O<sub>3</sub>, CaCO<sub>3</sub>, MoO<sub>3</sub>, Tm<sub>2</sub>O<sub>3</sub>, and Yb<sub>2</sub>O<sub>3</sub> were used as received without further purification. The raw materials were homogenized in absolute ethanol using an agate mortar and pestle for 4 hours to ensure uniform mixing. The mixture was first pre-sintered at 500 °C for 12 hours to decompose carbonates and initiate phase formation, followed by a second sintering step at 900 °C for 10 hours in air to enhance crystallinity. The resulting powder was collected and subjected to structural and optical characterizations.

### Characterization

The structural properties of the LCLMO:Tm<sup>3+</sup>/Yb<sup>3+</sup> phosphors were analyzed *via* X-ray diffraction (XRD) using a Bruker D8-Advance diffractometer with monochromatic Cu Kα<sub>1</sub> radiation (λ = 1.5406 Å) in the 2θ range of 10°–70°. Morphological characterization was performed using a Zeiss Supra55VP field-emission scanning electron microscope (FE-SEM) coupled with a Bruker XFlash 5030 energy-dispersive X-ray (EDX) detector for elemental mapping.

### Optical measurements

UV-Vis-NIR absorption spectra were recorded on a PerkinElmer Lambda 365 spectrophotometer and the UC luminescence spectra were measured using an Avantes high-resolution CCD detector under 975 nm excitation from a Spectra Physics 3900S tunable Ti:Sapphire laser. Temperature-dependent measurements were conducted using a Linkam THMS600 heating stage. The temporal decay profiles were captured with a 200 MHz LeCroy WS424 oscilloscope and a Hamamatsu R928 photomultiplier tube (PMT), excited by a 10 Hz EKSP/LA/NT342/3/UVE pulsed laser (OPO system, 10 ns pulse width).

### Penetration depth studies

To evaluate tissue penetration capabilities, the phosphor was excited at 975 nm using a Spectra Physics 3900S Ti:Sapphire laser, and emissions from the <sup>3</sup>H<sub>4</sub> → <sup>3</sup>H<sub>6</sub> transition (first biological window) were detected through a blood phantom. A cooled Newton DU920 N CCD detector (0.7 nm resolution, 1 s integration time) measured the emission intensity as a function of penetration depth.

## Results and discussion

### Structural and morphological characterization

Fig. 1 presents the XRD pattern of the LCLMO:Tm<sup>3+</sup>/Yb<sup>3+</sup> phosphor, which closely aligns with the simulated diffraction profile of the tetragonal LCLMO host lattice (space group *I*<sub>4</sub>/a).<sup>21</sup> All reflections are indexed to the tetragonal unit cell, confirming phase purity and crystallinity. The absence of secondary phases in the experimental pattern verifies successful doping and structural stability.

Rietveld refinement Fig. 2a was performed to refine the crystallographic parameters. The optimized unit cell dimensions are: *a* = *b* = 5.2529 Å, *c* = 11.4888 Å, and the Unit cell volume = 316.53 Å<sup>3</sup>. The refinement confirms a pure tetragonal



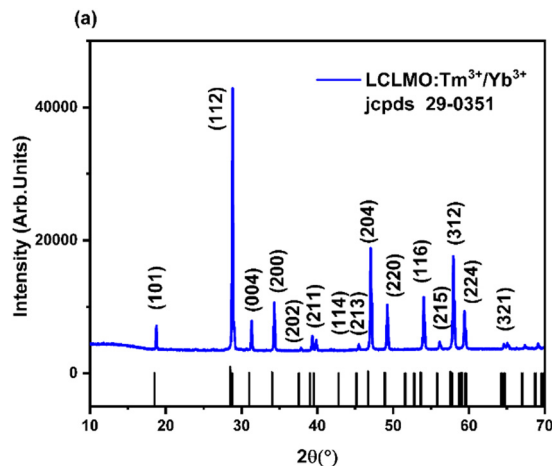


Fig. 1 XRD patterns of the Particle LCLMO:Tm<sup>3+</sup>/Yb<sup>3+</sup>.

phase with  $R$ -factors ( $R_p = 3.2\%$ ,  $R_{wp} = 4.1\%$ ) indicative of a high-quality fit. No detectable impurities or structural defects were observed, corroborating the effectiveness of the solid-state synthesis route.

The SEM images reveal that the LCLMO:Tm<sup>3+</sup>/Yb<sup>3+</sup> phosphor exhibits agglomerated particles with irregular morphologies shown in Fig. 2b. The particle sizes range from 1  $\mu\text{m}$  to several micrometers, indicating non-uniform growth during synthesis. This agglomeration and broad size distribution may limit the effective light-emission surface area and reduce packing density, potentially impacting luminescent efficiency and application performance in devices requiring uniform particle distribution.

### Optical characterization

Fig. 3a displays the diffuse reflectance spectra of LCLMO:Tm<sup>3+</sup>/Yb<sup>3+</sup> phosphors in the 200–1100 nm range. The spectrum reveals a strong absorption band at 280 nm, attributed to the  $\text{O}^{2-} \rightarrow \text{Mo}^{6+}$  charge transfer transition within the  $\text{MoO}_4^{2-}$  groups.<sup>22</sup> Characteristic absorption peaks of Tm<sup>3+</sup> are observed at 472 nm ( $^1\text{G}_4 \leftarrow ^3\text{H}_6$ ), 688 nm ( $^3\text{F}_2 \leftarrow ^3\text{H}_6$ ), and 795 nm

( $^3\text{H}_4 \leftarrow ^3\text{H}_6$ ), while a broad absorption band centered at 975 nm corresponds to the  $^2\text{F}_{7/2} \rightarrow ^2\text{F}_{5/2}$  transition of Yb<sup>3+</sup>.<sup>23</sup>

### Band gap determination

Fig. 3b displays the optical band gap of LCLMO:Tm<sup>3+</sup>/Yb<sup>3+</sup> was calculated using Kubelka–Munk (KM) theory. By plotting  $[F(R_\infty)h\nu]^2$  against photon energy ( $h\nu$ ) and extrapolating the linear region to  $[F(R_\infty)h\nu]^2 = 0$ , the band gap energy ( $E_g$ ) was determined to be 3.22 eV. This value aligns with the semiconducting nature of molybdate-based hosts and confirms their suitability for near-infrared (NIR) applications.

### Photoluminescence at room temperature

Fig. 4a displays the luminescence's spectrum profile with the excitation of 975 nm of LCLMO co-doped Tm<sup>3+</sup>/Yb<sup>3+</sup>. The three different emission peaks that constitute the luminescence spectrum are 475, 650, and 800 nm. All these emissions are attributed to the Tm<sup>3+</sup> ions, resulting from the energy transfer from Yb<sup>3+</sup> to Tm<sup>3+</sup>. Specifically, the 475 nm and 800 nm fluorescence bands correspond to the  $^1\text{G}_4 \rightarrow ^3\text{H}_6$  and  $^3\text{H}_4 \rightarrow ^3\text{H}_6$  respective transitions. Furthermore, emission at 650 nm is associated with  $^1\text{G}_4 \rightarrow ^3\text{F}_4$  transitions, as has been widely discussed in previous studies.<sup>24</sup> The blue emission attributed to the  $^1\text{G}_4 \rightarrow ^3\text{H}_6$  transition is recorded with a sufficient intensity in Tm<sup>3+</sup>/Yb<sup>3+</sup> doped phosphors, although in this material this intensity is considered to be too low in comparison with the NIR band. As shown in Fig. 4b, the final color is blue with CIE chromaticity parameters ( $x = 0.1801$ ,  $y = 0.1737$ ).

Furthermore, the decay times for Tm<sup>3+</sup>/Yb<sup>3+</sup> doped LCLMO recorded at 975 nm excitation are displayed in Fig. 5. These curves are the characteristics of up conversion processes, and the temporal evolution is a function of the lifetimes of the levels involved in the UC mechanism.

As can be shown, the rising component of the recorded decay curves contributes significantly, suggesting the presence of energy-transfer UC mechanisms that are required to fill this level. The effective lifetime was calculated using the average

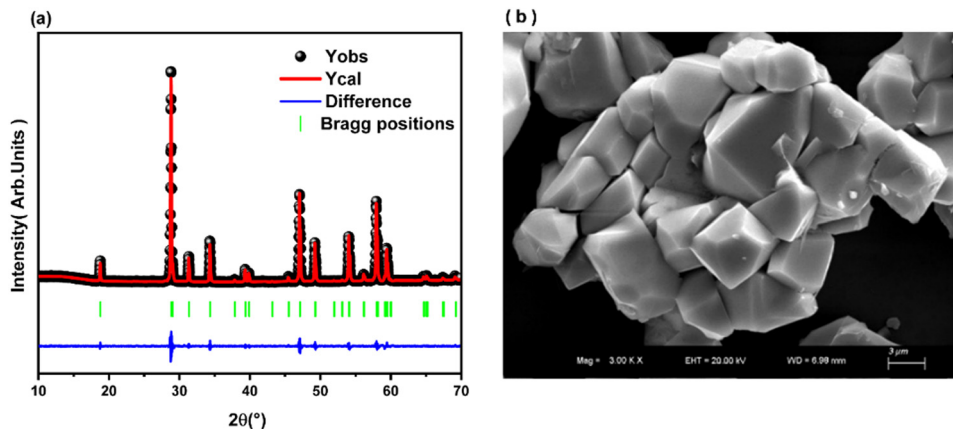


Fig. 2 (a) Rietveld refinement of the XRD pattern with  $\chi^2 = 1.32$  and  $R_{wp} = 9.63$ , (b) SEM image of  $\text{LiCaLa}(\text{MoO}_4)_3:\text{Tm}^{3+}/\text{Yb}^{3+}$  particles showing the surface morphology.



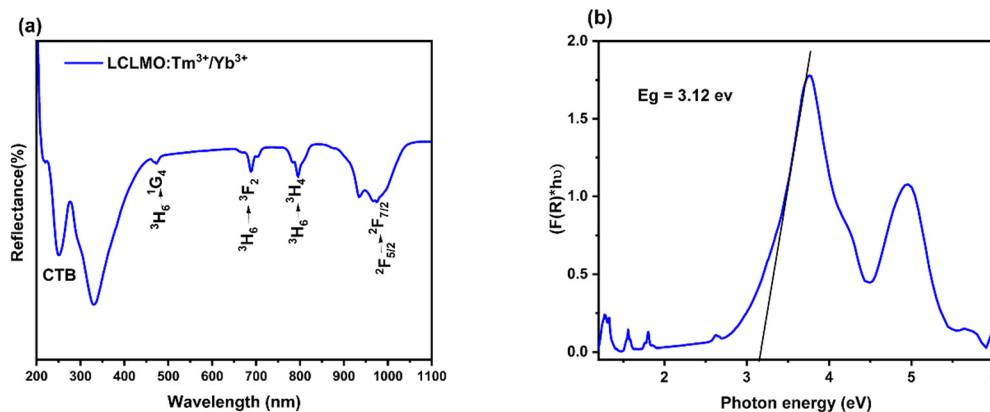


Fig. 3 (a) Diffuse reflectance spectra of  $\text{LiCaLa}(\text{MoO}_4)_3:\text{Tm}^{3+}/\text{Yb}^{3+}$  phosphors. (b) Tauc plot used to estimate the optical band gap of the doped samples.

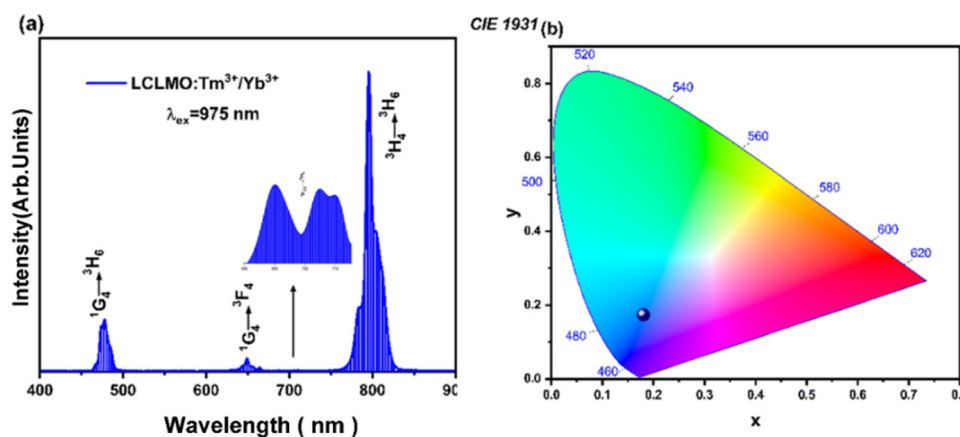


Fig. 4 (a) Upconversion emission spectra of  $\text{LiCaLa}(\text{MoO}_4)_3:\text{Tm}^{3+}/\text{Yb}^{3+}$  phosphors under 975 nm excitation. (b) Corresponding CIE 1931 chromaticity diagram showing the emission color coordinates of the doped sample.

lifetime formula:<sup>25</sup>

$$\tau = \frac{\int tI dt}{\int I dt} \quad (1)$$

where  $t$  is the time and  $I(t)$  is the emission intensity. The emission at 475 nm, corresponding to the  $^1\text{G}_4 \rightarrow ^3\text{H}_6$  transition of  $\text{Tm}^{3+}$ , exhibited a lifetime of 0.14 ms, while the emission at 800 nm, assigned to the  $^3\text{H}_4 \rightarrow ^3\text{H}_6$  transition, showed a longer lifetime of 0.3 ms. These values are consistent with previously reported data in the literature for similar  $\text{Tm}^{3+}/\text{Yb}^{3+}$  systems, indicating efficient energy transfer from  $\text{Yb}^{3+}$  to  $\text{Tm}^{3+}$  and successful population of the higher excited states (*via* up conversion processes).

To explore the transition processes of the different emission peaks, the link between the luminous intensity of the blue and NIR emissions of the LCLMO-doped  $\text{Tm}^{3+}/\text{Yb}^{3+}$  phosphor and the power of the pump is described in Fig. 6a. In general, the number of photons required to occupy the higher states for UC processes may be calculated using the following equation:<sup>26,27</sup>

$$I = K \times P^n \quad (2)$$

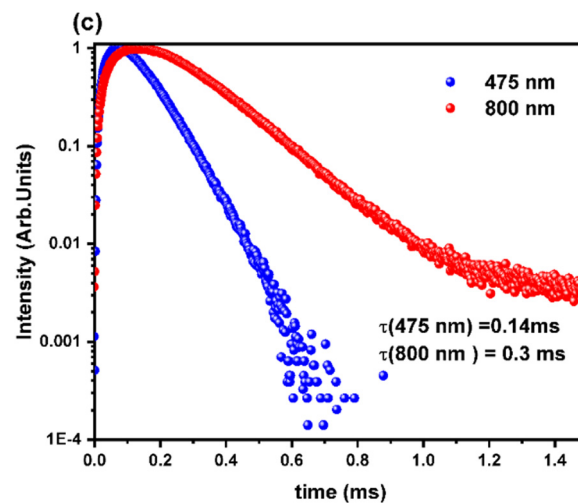


Fig. 5 Luminescence decay curve of  $\text{LiCaLa}(\text{MoO}_4)_3:\text{Tm}^{3+}/\text{Yb}^{3+}$  phosphors under 975 nm excitation, showing the temporal evolution of the emission intensity.



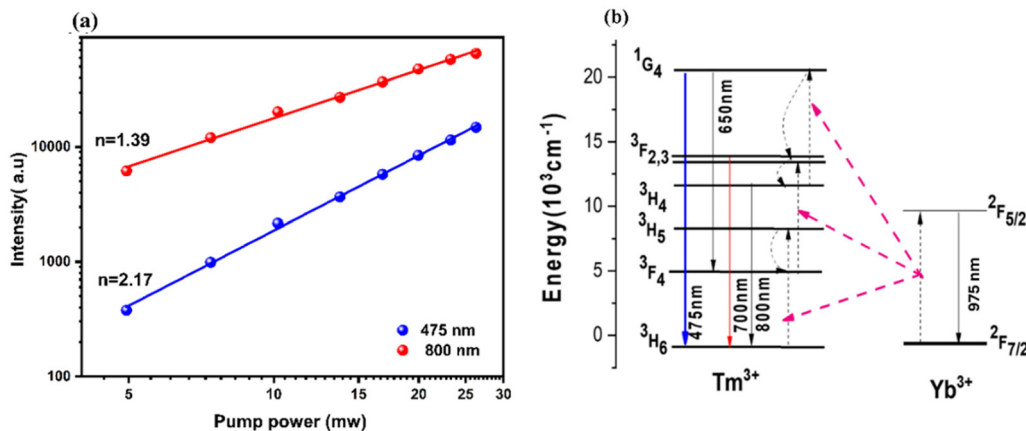


Fig. 6 (a) Upconversion emission intensity of  $\text{LiCaLa}(\text{MoO}_4)_3:\text{Tm}^{3+}/\text{Yb}^{3+}$  phosphors as a function of pump power under 975 nm excitation. (b) Schematic energy level diagram of  $\text{Tm}^{3+}$  and  $\text{Yb}^{3+}$  ions illustrating the upconversion mechanism in the LCLMO host matrix.

where  $I$ , is the intensity,  $P$  is the laser pump power and  $n$  is the number of photons. From the experimental data reported in Fig. 6a, the slope is 2.17 for blue emission and 1.39 for NIR emission. Using these numbers, two photons are utilized in the NIR emission UC process, whereas three photons are used in the blue UC. Fig. 6b presents a schematic, simplified depiction of the primary radiative and nonradiative processes occurring in the studied system.<sup>28</sup> The excited  $\text{Yb}^{3+}$  ions play a critical part in the energy transfer process. They transfer their energy to the  $\text{Tm}^{3+}$  ions, elevating them from the ground  $^3\text{H}_6$  level to the excited  $^3\text{H}_5$  level. Subsequently, the  $\text{Tm}^{3+}$  ions undergo non-radiative relaxation, populating the  $^3\text{F}_4$  level. In the next stage, newly excited  $\text{Yb}^{3+}$  ions contribute their energy to pump the  $\text{Tm}^{3+}$  ions to the  $^3\text{F}_4$  level, facilitating the population of the  $^3\text{F}_2$  and  $^3\text{F}_3$  levels. The  $\text{Tm}^{3+}$  ions within the  $^3\text{F}_2$  and  $^3\text{F}_3$  levels then experience non-radiative relaxation to the  $^3\text{H}_4$  level. The  $\text{Yb}^{3+}$  ions subsequently transfer their energy to excite the  $\text{Tm}^{3+}$  ions to the  $^3\text{H}_4$  level, from which they populate the  $^1\text{G}_4$  level. Finally, the excited  $\text{Tm}^{3+}$  ions residing in the  $^1\text{G}_4$  level transition back to the ground state  $^3\text{H}_6$ , generating blue light at approximately 475 nm. Additionally, a tiny percentage of the excited ions

undergo relaxation to the  $^3\text{F}_4$  level, resulting in the emission of red light at roughly 654 nm. From the intermediate level  $^3\text{H}_4$  level also occurs the emission at 800 nm corresponding to the  $^3\text{H}_4 \rightarrow ^3\text{H}_6$  transition.<sup>29–31</sup>

### Thermal sensing performance at high-temperature

Reliable temperature monitoring is crucial for practical applications since temperature is an important metric in scientific study, health care, and industry. First, it is crucial to highlight that LCLMO was selected as a host for optically active lanthanide ions owing to its resilience to high-temperature treatment and the capacity to be doped with different lanthanide ions. This resulted in a well-crystallized sample with micro-sized particles and vivid, strong fluorescence.

Fig. 7a displays UC spectra with increasing temperature in the range (298–748 K) using 975 nm excitation with 5 mw power to remove the photo-thermal effect. Due to thermal quenching processes, the intensity  $^1\text{G}_4 \rightarrow ^3\text{H}_6$ ;  $^3\text{H}_4 \rightarrow ^3\text{H}_6$  and  $^1\text{G}_4 \rightarrow ^3\text{F}_4$  of  $\text{Tm}^{3+}$  peaks decreases with increasing temperature, with the exception of the thermalized band  $^2\text{F}_{2,3} \rightarrow ^3\text{H}_6$  around 700 nm, which increases with temperature.<sup>32</sup> The change in color with

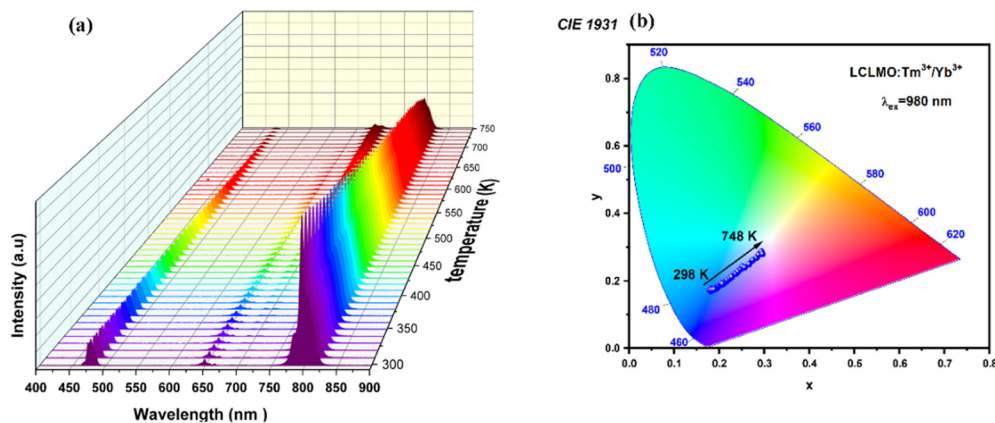


Fig. 7 (a) Temperature-dependent upconversion emission spectra of  $\text{LiCaLa}(\text{MoO}_4)_3:\text{Tm}^{3+}/\text{Yb}^{3+}$  phosphors recorded in the range 298 K to 748 K under 975 nm excitation. (b) Corresponding CIE chromaticity diagram showing the variation of emission color with temperature.



the change in temperature is compatible with the chromaticity coordinates as seen in the CIE diagram (Fig. 7b), These findings show that the LCLMO:Yb<sup>3+</sup>/Tm<sup>3+</sup> materials may be utilized as visual optical temperature sensors, taking advantage of their thermochromic features. In addition, the LCLMO:Yb<sup>3+</sup>/Tm<sup>3+</sup> materials may be employed for safety signs in high temperature situations because to their temperature-sensitive and adaptable luminescence.

For temperature sensing applications, we will focus on two different band intensity ratios corresponding to the thermally coupled levels (TCL) of Tm<sup>3+</sup>. In this context, the thermally coupled levels (TCL) between the <sup>3</sup>F<sub>2,3</sub> and <sup>3</sup>H<sub>4</sub> of Tm<sup>3+</sup>. Usually these levels are located at an energy separation about (1500–2000 cm<sup>-1</sup>).<sup>33</sup> As the temperature rises, the intensity of the I<sub>2</sub> (700 nm) increases, and the intensity of the I<sub>1</sub> (800 nm) decreases, following the Boltzmann distribution.<sup>34</sup>

$$\text{FIR}_{\text{TCL}} = \frac{I_2}{I_1} = B \times \exp\left(\frac{-\Delta E}{k_B T}\right) \quad (3)$$

where  $A$  is a parameter that depends on the host lattice,  $T$  is the absolute temperature,  $k$  is the Boltzmann constant, and  $\Delta E$  is the energy gap between these two thermalized states.

Fig. 8a shows the temperature variation of the FIR (700/800) value in the range 298–748 K. By using eqn (3), we have obtained a correlation between the calculated 700/800 band intensity ratio and temperature, resulting in a  $\Delta E = 1577.52 \text{ cm}^{-1}$ .

Furthermore, the intensity of the blue emission provides a useful reference in optical thermal sensor in the range 298–748 K. The high energy differences in NTCELs are a problem for thermal excitation. As a result, conventional FIR is not applicable to NTCLs for large values of  $\Delta E$ . In the absence of a well-defined physical model that accurately describes the temperature dependencies of FIR values for Ln<sup>3+</sup> NTCELs, an empirical approach becomes crucial to capture the complex variations observed in the experimental data. Consequently, the experimental data of the FIR<sub>NTCL</sub> (700/475) shown in Fig. 8b, were fitted with the following function:<sup>35</sup>

$$\text{FIR}_{\text{NTCL}} = \frac{I_1}{I_2} = A \times \exp\left(\frac{T}{B}\right) + C \quad (4)$$

where  $A$ ,  $B$  and  $C$  are constants.

### Thermal sensing performance analysis

Sensitivity was a crucial and notable attribute when it came to quantitatively evaluating the appropriateness of materials for use as optical sensors in real-world applications. Moreover, the absolute sensitivity ( $S_a$ ) and relative sensitivity ( $S_r$ ) can be computed using the following formula. These sensitivities are defined by these two equations:

$$S_a = \partial \text{FIR} / \partial T \quad (5)$$

$$S_r = \frac{1}{\text{FIR}} \times \frac{\partial \text{FIR}}{\partial T} \times 100\% \quad (6)$$

It's observed that in all cases, regardless of whether it is TCL and NTCL, the absolute sensitivity increases with the rise in temperature, with a maximum of  $7.66 \times 10^{-4}$  and  $6.2 \times 10^{-2}$  respectively.

As illustrated in Fig. 9a, the relative sensitivity achieves a maximum of  $2.62\% \text{ K}^{-1}$  at 298 K. It is important to note that as the temperature increases, there is a decrease in relative sensitivity, and the value at 750 K is  $0.5\% \text{ K}^{-1}$ . Using eqn (4) it is significant that the relative sensitivity increases as the temperature increases as shown in Fig. 9b and the value at 748 K is  $1.4\% \text{ K}^{-1}$ . Currently, our developed sensor is likely the most sensitive ( $1.4\% \text{ K}^{-1}$ ) at high temperatures out of all the luminescent thermometers available.<sup>24,32,36</sup>

Table 1 compares the maximum relative temperature sensitivity ( $S_{r,\text{max}}$ ) and temperature uncertainty of LCLMO:Yb<sup>3+</sup>/Tm<sup>3+</sup> with other Tm<sup>3+</sup>/Yb<sup>3+</sup> doped matrices reported in the literature. The results demonstrate that the developed thermometer exhibits exceptional performance in high-temperature industrial applications (up to 748 K). Notably:

- At moderate temperatures (298 K): utilizing Tm<sup>3+</sup> thermally coupled levels (TCLs) yields an ultrahigh  $S_{r,\text{max}}$  of  $2.62\% \text{ K}^{-1}$ , surpassing most literature values.
- At extreme temperatures (748 K): a record  $S_{r,\text{max}}$  of  $1.4\% \text{ K}^{-1}$  is achieved *via* non-thermally coupled levels (NTCLs), outperforming systems where sensitivity typically drops to  $0.1\text{--}0.3\% \text{ K}^{-1}$  at high temperatures.

To clarify the advantages of our host matrix, we compared the performance of LiCaLa(MoO<sub>4</sub>)<sub>3</sub>:Tm<sup>3+</sup>/Yb<sup>3+</sup> with previously

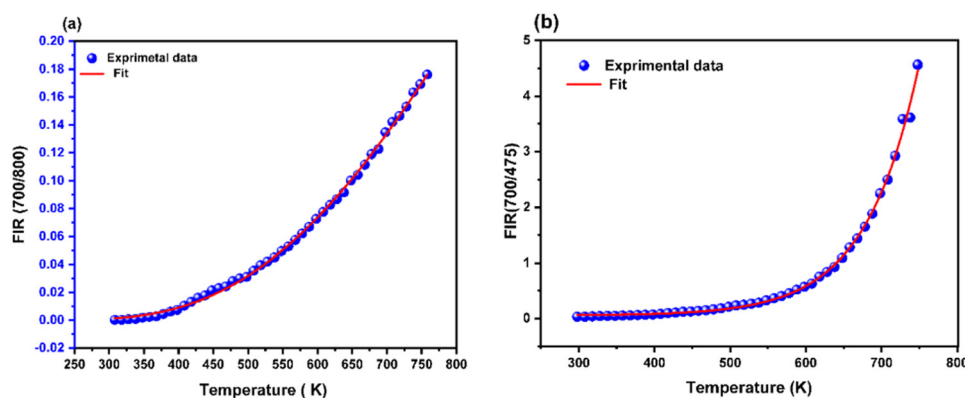


Fig. 8 Experimental fluorescence intensity ratio (FIR) as a function of temperature (298–748 K) for LiCaLa(MoO<sub>4</sub>)<sub>3</sub>:Tm<sup>3+</sup>/Yb<sup>3+</sup> phosphors: (a) FIR based on thermally coupled levels (TCL) at 700 nm and 800 nm. (b) FIR based on non-thermally coupled levels (NTCL) at 700 nm and 475 nm.



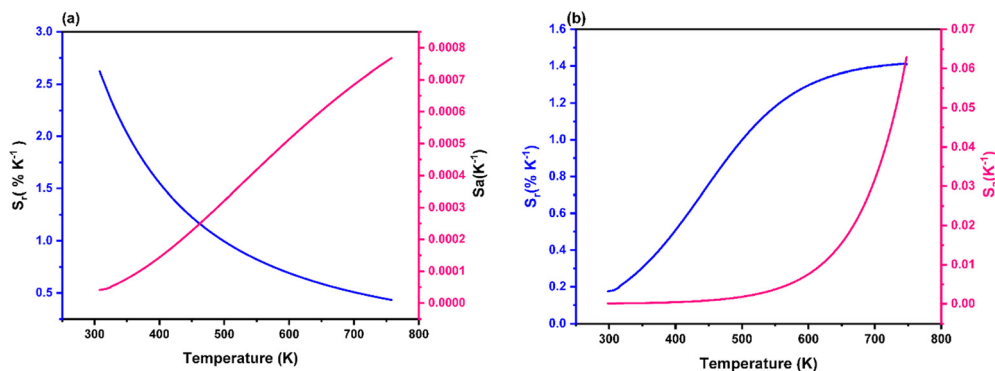


Fig. 9 Calculated absolute sensitivity ( $S_a$ ) and relative sensitivity ( $S_r$ ) of LiCaLa(MoO<sub>4</sub>)<sub>3</sub>:Tm<sup>3+</sup>/Yb<sup>3+</sup> phosphors in the temperature range 298–748 K, based on: (a) thermally coupled levels (TCL) using the emission intensity ratio at 700 nm and 800 nm. (b) Non-thermally coupled levels (NTCL) using the emission intensity ratio at 700 nm and 475 nm.

Table 1 Sensitivity and temperature range of the sensor material at high-Temperature

Materials	$T$ range (K)	$S_r$ (% K <sup>-1</sup> ) at 300 K	$S_r$ (% K <sup>-1</sup> ) at $T_{max}$	$\delta T$ (K)	Ref.
NaY <sub>2</sub> F <sub>7</sub> :Tm <sup>3+</sup> /Yb <sup>3+</sup>	300–567	0.5	1.63 (415 K)	—	43
Na <sub>3</sub> GdV <sub>2</sub> O <sub>8</sub> :Tm <sup>3+</sup> /Yb <sup>3+</sup>	298–565	1.34	2.01 (565 K)	0.4	36
Ba <sub>2</sub> GdV <sub>3</sub> O <sub>11</sub> :Tm <sup>3+</sup> /Yb <sup>3+</sup>	303–603	1.5	1.7 (350 K)	0.35	24
YVO <sub>4</sub> :Tm <sup>3+</sup> /Yb <sup>3+</sup>	300–1009	2.86	2.86 (300 K)	0.15	32
YPO <sub>4</sub> :Tm <sup>3+</sup> /Yb <sup>3+</sup>	293–773	2.40	2.4 (293 K)	—	44
GdVO <sub>4</sub> :Tm <sup>3+</sup> /Yb <sup>3+</sup>	297–673	0.19	0.20 (673 K)	11	45
LiCaLa(MoO <sub>4</sub> ) <sub>3</sub> :Tm <sup>3+</sup> /Yb <sup>3+</sup>	298–748 (NTCL)	0.17	<b>1.4 (748 K)</b>	0.3	<b>This work</b>
LiCaLa(MoO <sub>4</sub> ) <sub>3</sub> :Tm <sup>3+</sup> /Yb <sup>3+</sup>	298–748 (TCL)	2.62	2.89 (298 K)	0.4	<b>This work</b>

reported systems such as YVO<sub>4</sub>-based phosphors.<sup>34</sup> Although the energy gap between the relevant thermally coupled levels (<sup>3</sup>F<sub>2</sub> and <sup>3</sup>H<sub>4</sub>) in LCLMO (1577 cm<sup>-1</sup>) is slightly smaller than that in YVO<sub>4</sub> (1777 cm<sup>-1</sup>), LCLMO offers several distinct benefits: (i) a broader and more intense emission band at 800 nm, falling within the second near-infrared window (NIR-II), which supports enhanced tissue penetration; (ii) improved chemical and thermal robustness due to the molybdate-based double perovskite-like structure, crucial for biological applications; and (iii) strong emission intensity even at relatively low excitation powers, reducing potential phototoxicity. These features position LCLMO as a promising alternative for multifunctional bioimaging and optical thermometry platforms.

### Temperature resolution

However, temperature resolution ( $\delta T$ ), the minimum detectable temperature change, serves as a critical metric for evaluating sensor efficacy. This parameter depends on both the material's intrinsic properties (*e.g.*,  $S_r$ ) and external factors such as signal-to-noise ratio (SNR) during calibration. To enhance resolution, strategies like extended integration times or multi-measurement averaging can reduce experimental noise. It is derived from the formula:<sup>37</sup>

$$\delta T = \frac{1}{S_r} \cdot \frac{\delta \text{FIR}}{\text{FIR}} \quad (7)$$

where  $\delta(\text{FIR})/\text{FIR}$  represents the relative uncertainty in the fluorescence intensity ratio (FIR), and  $S_r$  denotes thermal

sensitivity.  $\delta \text{FIR}/\text{FIR}$  can be expressed by this formula:

$$\frac{\delta \text{FIR}}{\text{FIR}} = \sqrt{2} \cdot \frac{\delta I}{I} \quad (8)$$

Here  $I$  is the integrated area of a peak and  $\delta I/I$  is determined from the signal to noise ratio values. Where  $(\delta I/I)$  are 0.73% in the case of TCL and is 0.04% in the case of NTCL.

Fig. 10a and b presents the computed temperature resolution across the 298–748 K range. For the TCL-based approach, the resolution varies between 0.3 and 2.0 K, while for the NTCL-based approach, it ranges from 0.32 to 0.04 K over the same temperature range. Notably, the NTCL method achieves exceptional resolution, underscoring its superior precision.

To evaluate the limit of detection, also known as experimental temperature uncertainty which represents the lowest possible temperature variation which could be detected during a specific measurement, 100 repeated spectra were recorded at 298 K (Fig. 11a and b). The temperature estimates followed a Gaussian distribution, yielding standard deviations of 0.4 K (TCLs) and 0.3 K (NTCLs).<sup>38</sup> These findings confirm that the LCLMO:Tm<sup>3+</sup>/Yb<sup>3+</sup> thermometer meets the stringent requirements for dual-use applications in biomedical and industrial thermal monitoring. Our findings show that LCLMO:Tm<sup>3+</sup>/Yb<sup>3+</sup> upconverting materials have a high degree of sensitivity to thermal changes and low error in temperature readings, making them ideal for optical thermometry utilizing the FIR approach.



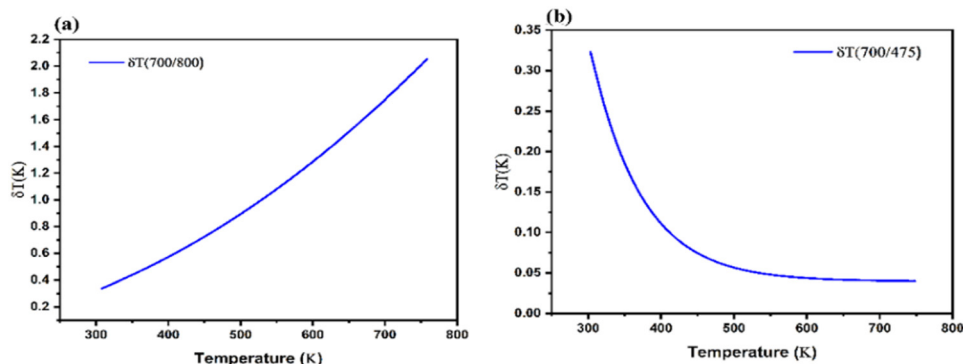


Fig. 10 Temperature resolution of LCLMO doped  $\text{Tm}^{3+}/\text{Yb}^{3+}$  (a) TCL 700/800 (b) NTCL 700/475.

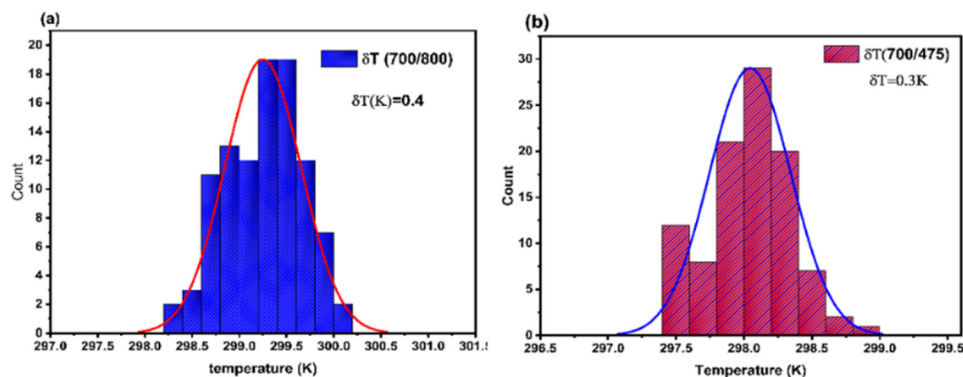


Fig. 11 Histograms of temperature distribution obtained from 100 repeated measurements (a) TCL 700/800 (b) NTCL 700/475, at room temperature of LCLMO doped  $\text{Tm}^{3+}/\text{Yb}^{3+}$  at room temperature.

Compared to conventional ceramic-based phosphors  $\text{La}_2(\text{MoO}_4)_3:\text{Yb}^{3+}/\text{Ho}^{3+}/\text{Er}^{3+}$ ,<sup>39</sup>  $\text{NaSrY}(\text{MoO}_4)_3:\text{Er}^{3+}/\text{Tm}^{3+}/\text{Yb}^{3+}$ ,<sup>40</sup>  $\text{NaCaY}(\text{MoO}_4)_3:\text{Pr}^{3+}$ ,<sup>41</sup> and  $\text{Y}_2\text{Mo}_3\text{O}_{12}:\text{Pr}^{3+}/\text{Yb}^{3+}$ ,<sup>42</sup> this material demonstrates superior resolution within its operational temperature range, underscoring its potential for high-precision sensing.

Repeatability ( $R$ ) is another crucial metric for assessing the accuracy of the temperature sensing techniques employed. The thermometric parameters, specifically the FIR values, were

measured multiple times as the sample was cycled from a low to a high temperature, as illustrated in Fig. 12(a) and (b). The repeatability ( $R$ ) was calculated using the following

$$R_p(100\%) = \left( \frac{1 - |M_i(T)c - M(T)c|}{\text{FIR}c} \right) \times 100$$

where  $M_i(T)c$  is the measured parameter (FIR or band centroid) in the  $i$ th cycle and  $M(T)c$  is the mean value of the  $M(T)$  cover 10 cycles. The FIR values determined change reversibly with

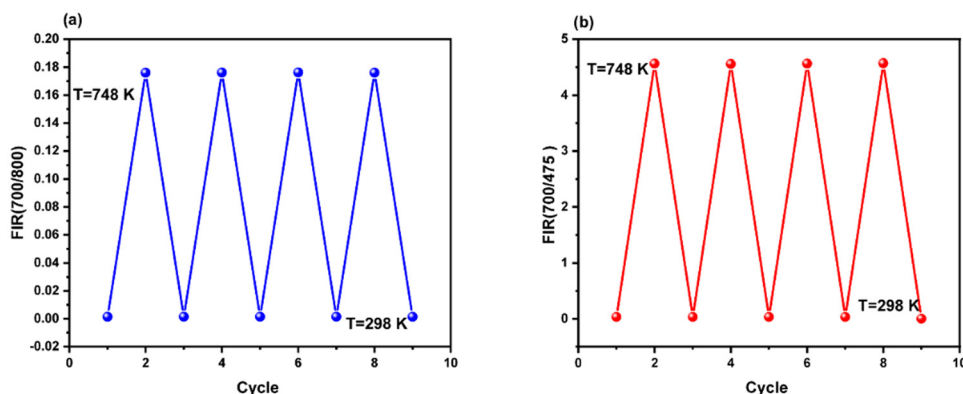


Fig. 12 Repeatability assessment ( $R$ ) (a) (700/800) (b) (700/475) for LCLMO doped  $\text{Tm}^{3+}/\text{Yb}^{3+}$ .



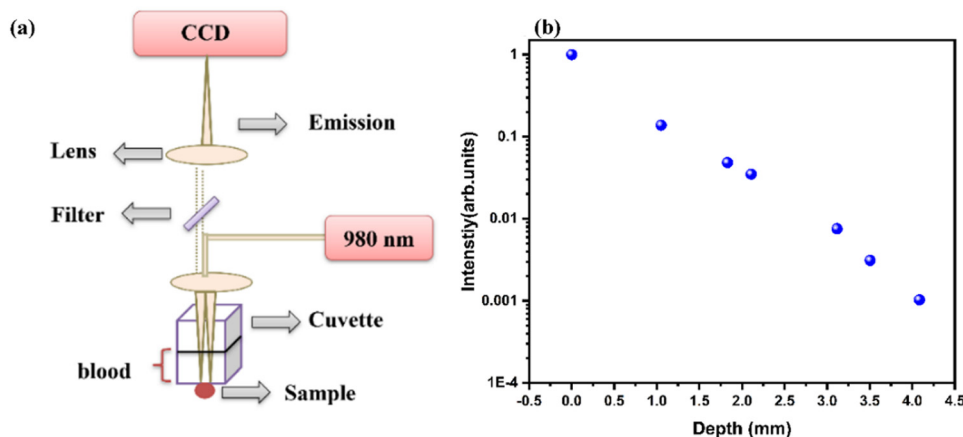


Fig. 13 (a) Experimental procedures for determining the depth of penetration (b) luminescence intensity as a function of the depth of the blood as obtained for the emission of 800 nm of LCLMO doped  $\text{Tm}^{3+}/\text{Yb}^{3+}$  with 975 nm excitation.

temperature, and the FIR values for all FIRs were above 97% over the 298–748 K temperature range, confirming the good repeatability and reliability of the thermometric methods applied.

### Analysis of application in biomedical experiments

To evaluate the potential of LCLMO: $\text{Tm}^{3+}/\text{Yb}^{3+}$  in biomedical imaging, a vertical experimental setup (Fig. 9a) was designed to simulate *in vivo* excitation conditions.<sup>46,47</sup> Human blood with anticoagulant, was placed in a cuvette positioned above a specialized container holding the phosphor. With this setup is simulated an excitation and a detection of LCLMO: $\text{Tm}^{3+}/\text{Yb}^{3+}$  inside of a biological system. Under continuous 975 nm laser excitation, the emission intensity at 800 nm ( $\text{Tm}^{3+}:^3\text{H}_4 \rightarrow ^3\text{H}_6$  transition) was monitored as a function of blood depth. Fig. 9b reveals an exponential decay in signal intensity with increasing blood thickness, attributed to absorption and scattering losses. Despite this attenuation, the phosphor achieved a penetration depth of  $\sim 4$  mm in the first biological window (IBW, 650–1000 nm), demonstrating its feasibility for deep-tissue imaging and luminescence-based thermal sensing in biological environments. Combined with its exceptional thermal sensitivity ( $2.62\% \text{ K}^{-1}$  at 298 K), these results position LCLMO: $\text{Tm}^{3+}/\text{Yb}^{3+}$  as a dual-functional platform for non-invasive sub-tissue diagnostics and high-precision temperature monitoring in biomedical applications (Fig. 13).

## Conclusion

Luminescent materials have become essential for temperature sensing across various fields, from industrial catalysis to biomedical imaging. In this study, we demonstrate for the first time that lanthanide-doped up conversion (UC) phosphors,  $\text{LiCaLa}(\text{MoO}_4)_3:\text{Tm}^{3+}/\text{Yb}^{3+}$  (LCLMO), function as multifunctional optical sensors for both high-temperature monitoring (up to 748 K) and deep-tissue bioimaging within the first biological window (IBW, 650–1000 nm). By leveraging both thermally coupled levels (TCLs) and non-thermally coupled levels (NTCLs) under 975 nm excitation, LCLMO exhibits

exceptional thermal sensitivity:  $2.62\% \text{ K}^{-1}$  at 298 K for precise low-temperature detection and  $1.4\% \text{ K}^{-1}$  at 748 K for high-temperature resilience. Additionally, the material offers superior thermal resolution, ranging from 0.3 to 0.4 K across its operational temperature range, underscoring its potential for high-precision sensing. Our results confirm that LCLMO UC phosphors are highly suitable for optical thermometry *via* the fluorescence intensity ratio (FIR) approach, owing to their high thermal sensitivity and low temperature uncertainty at elevated temperatures (748 K). Furthermore, sub-tissue penetration studies using a blood phantom revealed a 4 mm penetration depth at 800 nm ( $^3\text{H}_4 \rightarrow ^3\text{H}_6$  transition), validating its capability for non-invasive bioimaging. However, we acknowledge that this material is not yet fully apt for biomedical applications. Further studies on biocompatibility, cytotoxicity, and long-term stability are required to meet the necessary biomedical standards. These findings establish LCLMO: $\text{Tm}^{3+}/\text{Yb}^{3+}$  as a versatile platform bridging advanced thermal sensing, with promising implications for next-generation diagnostics, therapeutics, and industrial monitoring.

## Data availability

All data underlying the results are available as part of the article and no additional source data are required.

## Conflicts of interest

There are no conflicts to declare.

## References

- X. Zhao, H. Suo, Z. Zhang and C. Guo, Upconverting  $\text{CeO}_2:\text{Yb}^{3+}/\text{Tm}^{3+}$  Hollow Nanospheres for Photo-Thermal Sterilization and Deep-Tissue Imaging in the First Biological Window, *Ceram. Int.*, 2019, **45**(17, Part A), 21910–21916, DOI: [10.1016/j.ceramint.2019.07.202](https://doi.org/10.1016/j.ceramint.2019.07.202).



- 2 R. P. Benedict, *Fundamentals of Temperature, Pressure, and Flow Measurements*, John Wiley & Sons, 1991.
- 3 L. Zhou, P. Du, W. Li, L. Luo and G. Xing, Composition Regulation Triggered Multicolor Emissions in  $\text{Eu}^{2+}$ -Activated  $\text{Li}_4(\text{Sr}_{1-x}\text{Ca}_{1+x})(\text{SiO}_4)_2$  for a Highly Sensitive Thermometer, *Ind. Eng. Chem. Res.*, 2020, **59**(21), 9989–9996, DOI: [10.1021/acs.iecr.0c00967](https://doi.org/10.1021/acs.iecr.0c00967).
- 4 C. Bouzigues, T. Gacoin and A. Alexandrou, Biological Applications of Rare-Earth Based Nanoparticles, *ACS Nano*, 2011, **5**(11), 8488–8505, DOI: [10.1021/nn202378b](https://doi.org/10.1021/nn202378b).
- 5 H. Cai, W. Lu, C. Yang, M. Zhang, M. Li, C.-M. Che and D. Li, Tandem Förster Resonance Energy Transfer Induced Luminescent Ratiometric Thermometry in Dye-Encapsulated Biological Metal–Organic Frameworks, *Adv. Opt. Mater.*, 2019, **7**(2), 1801149, DOI: [10.1002/adom.201801149](https://doi.org/10.1002/adom.201801149).
- 6 J. Liao, Z. Han, F. Lin, B. Fu, G. Gong, H. Yan, H. Huang, H.-R. Wen and B. Qiu, Simultaneous Thermal Enhancement of Upconversion and Downshifting Luminescence by Negative Thermal Expansion in Nonhygroscopic  $\text{ZrSc}(\text{WO}_4)_2\text{PO}_4:\text{Yb}/\text{Er}$  Phosphors, *Inorg. Chem.*, 2023, **62**(24), 9518–9527, DOI: [10.1021/acs.inorgchem.3c00880](https://doi.org/10.1021/acs.inorgchem.3c00880).
- 7 S. Tamboli, G. B. Nair, Z. Xia, S. J. Dhoble and H. C. Swart, Blue-Light Pumped NIR Emission of  $\text{LaOF}:\text{Pr}^{3+}$  Nanorods for Highly Sensitive Nanothermometry, *Ceram. Int.*, 2023, **49**(14, Part A), 23579–23590, DOI: [10.1016/j.ceramint.2023.04.192](https://doi.org/10.1016/j.ceramint.2023.04.192).
- 8 C. D. S. Brites, R. Marin, M. Suta, A. N. Carneiro Neto, E. Ximendes, D. Jaque and L. D. Carlos, Spotlight on Luminescence Thermometry: Basics, Challenges, and Cutting-Edge Applications, *Adv. Mater.*, 2023, **35**(36), 2302749, DOI: [10.1002/adma.202302749](https://doi.org/10.1002/adma.202302749).
- 9 M. A. Hernández-Rodríguez, A. D. Lozano-Gorrín, I. R. Martín, U. R. Rodríguez-Mendoza and V. Lavín, Comparison of the Sensitivity as Optical Temperature Sensor of Nano-Perovskite Doped with  $\text{Nd}^{3+}$  Ions in the First and Second Biological Windows, *Sens. Actuators, B*, 2018, **255**, 970–976, DOI: [10.1016/j.snb.2017.08.140](https://doi.org/10.1016/j.snb.2017.08.140).
- 10 C. Cressoni, F. Vurro, E. Milan, M. Muccilli, F. Mazzer, M. Gerosa, F. Boschi, A. E. Spinelli, D. Badocco, P. Pastore, N. Fernández Delgado, M. Herrera Collado, P. Marzola and A. Speghini, From Nanothermometry to Bioimaging: Lanthanide-Activated  $\text{KY}_3\text{F}_{10}$  Nanostructures as Biocompatible Multifunctional Tools for Nanomedicine, *ACS Appl. Mater. Interfaces*, 2023, **15**(98), 12171–12188, DOI: [10.1021/acsami.2c22000](https://doi.org/10.1021/acsami.2c22000).
- 11 N. Rakov,  $\text{Tm}^{3+}, \text{Yb}^{3+}:\text{Y}_2\text{SiO}_5$  up-Conversion Phosphors: Exploration of Temperature Sensing Performance by Monitoring the Luminescence Emission, *Phys. B*, 2022, **628**, 413572, DOI: [10.1016/j.physb.2021.413572](https://doi.org/10.1016/j.physb.2021.413572).
- 12 T. Grzyb, A. Gruszczyńska, R. J. Wiglusz and S. Lis, The Effects of Down- and up-Conversion on Dual-Mode Green Luminescence from  $\text{Yb}^{3+}$ - and  $\text{Tb}^{3+}$ -Doped  $\text{LaPO}_4$  Nanocrystals, *J. Mater. Chem. C*, 2013, **1**(34), 5410, DOI: [10.1039/c3tc31100g](https://doi.org/10.1039/c3tc31100g).
- 13 T. Grzyb, P. Kamiński, D. Przybylska, A. Tyimiński, F. Sanz-Rodríguez and P. Haro Gonzalez, Manipulation of Up-Conversion Emission in  $\text{NaYF}_4$  Core@shell Nanoparticles Doped by  $\text{Er}^{3+}$ ,  $\text{Tm}^{3+}$ , or  $\text{Yb}^{3+}$  Ions by Excitation Wavelength—Three Ions—Plenty of Possibilities, *Nanoscale*, 2021, **13**(15), 7322–7333, DOI: [10.1039/D0NR07136F](https://doi.org/10.1039/D0NR07136F).
- 14 S. Goderski, M. Runowski, P. Woźny, V. Lavín and S. Lis, Lanthanide Upconverted Luminescence for Simultaneous Contactless Optical Thermometry and Manometry—Sensing under Extreme Conditions of Pressure and Temperature, *ACS Appl. Mater. Interfaces*, 2020, **12**(36), 40475–40485, DOI: [10.1021/acsami.0c09882](https://doi.org/10.1021/acsami.0c09882).
- 15 N.-N. Dong, M. Pedroni, F. Piccinelli, G. Conti, A. Sbarbati, J. E. Ramírez-Hernández, L. M. Maestro, M. C. Iglesias-de la Cruz, F. Sanz-Rodríguez, A. Juarranz, F. Chen, F. Vetrone, J. A. Capobianco, J. G. Solé, M. Bettinelli, D. Jaque and A. Speghini, NIR-to-NIR Two-Photon Excited  $\text{CaF}_2:\text{Tm}^{3+}, \text{Yb}^{3+}$  Nanoparticles: Multifunctional Nanoprobes for Highly Penetrating Fluorescence Bio-Imaging, *ACS Nano*, 2011, **5**(11), 8665–8671, DOI: [10.1021/nn202490m](https://doi.org/10.1021/nn202490m).
- 16 H. Söderlund, M. Mousavi, H. Liu and S. Andersson-Engels, Increasing Depth Penetration in Biological Tissue Imaging Using 808-Nm Excited  $\text{Nd}^{3+}/\text{Yb}^{3+}/\text{Er}^{3+}$ -Doped Upconverting Nanoparticles, *J. Biomed. Opt.*, 2015, **20**(8), 086008, DOI: [10.1117/1.JBO.20.8.086008](https://doi.org/10.1117/1.JBO.20.8.086008).
- 17 Q. Zhan, J. Qian, H. Liang, G. Somesfalean, D. Wang, S. He, Z. Zhang and S. Andersson-Engels, Using 915-Nm Laser Excited  $\text{Tm}^{3+}/\text{Er}^{3+}/\text{Ho}^{3+}$ -Doped  $\text{NaYbF}_4$  Upconversion Nanoparticles for in Vitro and Deeper in Vivo Bioimaging without Overheating Irradiation, *ACS Nano*, 2011, **5**(5), 3744–3757, DOI: [10.1021/nn200110j](https://doi.org/10.1021/nn200110j).
- 18 Y. Dai, D. Yang, P. Ma, X. Kang, X. Zhang, C. Li, Z. Hou, Z. Cheng and J. Lin, Doxorubicin Conjugated  $\text{NaYF}_4:\text{Yb}^{3+}/\text{Tm}^{3+}$  Nanoparticles for Therapy and Sensing of Drug Delivery by Luminescence Resonance Energy Transfer, *Biomaterials*, 2012, **33**(33), 8704–8713, DOI: [10.1016/j.biomaterials.2012.08.029](https://doi.org/10.1016/j.biomaterials.2012.08.029).
- 19 O. Savchuk, J. J. Carvajal Marti, C. Cascales, P. Haro-Gonzalez, F. Sanz-Rodríguez, M. Aguilo and F. Diaz, Bifunctional  $\text{Tm}^{3+}, \text{Yb}^{3+}:\text{GdVO}_4@ \text{SiO}_2$  Core-Shell Nanoparticles in HeLa Cells: Upconversion Luminescence Nanothermometry in the First Biological Window and Biolabelling in the Visible, *Nanomaterials*, 2020, **10**(5), 993, DOI: [10.3390/nano10050993](https://doi.org/10.3390/nano10050993).
- 20 H. Suo, F. Hu, X. Zhao, Z. Zhang, T. Li, C. Duan, M. Yin and C. Guo, All-in-One Thermometer-Heater up-Converting Platform  $\text{YF}_3:\text{Yb}^{3+}, \text{Tm}^{3+}$  Operating in the First Biological Window, *J. Mater. Chem. C*, 2017, **5**(6), 1501–1507, DOI: [10.1039/C6TC05449H](https://doi.org/10.1039/C6TC05449H).
- 21 P. Sharma, J. P. Madda and S. Vaidyanathan, Narrow-Band Dazzling Red-Emitting ( $\text{LiCaLa}(\text{MoO}_4)_3:\text{Eu}^{3+}$ ) Phosphor with Scheelite Structure for Hybrid White LEDs and  $\text{LiCaLa}(\text{MoO}_4)_3:\text{Sm}^{3+}, \text{Eu}^{3+}$ -Based Deep-Red LEDs for Plant Growth Applications, *Dalton Trans.*, 2023, **52**(41), 15043–15056, DOI: [10.1039/D3DT02716C](https://doi.org/10.1039/D3DT02716C).
- 22 Y. Bahrouni, I. Kachou, K. Saidi, T. Kallel, M. Dammak, I. Mediavilla and J. Jiménez, Enhancing the Luminescence Intensity of  $\text{Eu}^{3+}$ -Activated  $\text{NaYb}(\text{MoO}_4)_2$  Phosphors through Bismuth Doping: Judd–Ofelt Analysis, Lighting, and Temperature-Sensing Applications, *Mater. Adv.*, 2025, **6**, 1307, DOI: [10.1039/D4MA01167H](https://doi.org/10.1039/D4MA01167H).



- 23 K. Saidi, M. Dammak, K. Soler-Carracedo and I. R. Martín, A Novel Optical Thermometry Strategy Based on Emission of  $\text{Tm}^{3+}/\text{Yb}^{3+}$  Codoped  $\text{Na}_3\text{GdV}_2\text{O}_8$  Phosphors, *Dalton Trans.*, 2022, 51(13), 5108–5117, DOI: [10.1039/D1DT03747A](https://doi.org/10.1039/D1DT03747A).
- 24 I. Kachou, K. Saidi, C. Hernández-Álvarez, M. Dammak and I. R. Martín, Enhancing Thermometric Precision: Modulating the Temperature of Maximum Sensitivity via Erbium Dopant Addition in  $\text{Ba}_2\text{GdV}_3\text{O}_{11}:\text{Tm}^{3+}/\text{Yb}^{3+}$  Nano Phosphors, *Mater. Adv.*, 2024, 5(20), 8280–8293, DOI: [10.1039/D4MA00699B](https://doi.org/10.1039/D4MA00699B).
- 25 M. Fhoula, K. Saidi, C. Hernández-Álvarez, K. Soler-Carracedo, M. Dammak and I. R. Martín, Unlocking the Luminescent Potential of  $\text{Pr}^{3+}/\text{Yb}^{3+}$  Co-Doped  $\text{Y}_2\text{Mo}_4\text{O}_{15}$  for Advanced Thermometry Applications, *J. Alloys Compd.*, 2024, 979, 173537, DOI: [10.1016/j.jallcom.2024.173537](https://doi.org/10.1016/j.jallcom.2024.173537).
- 26 K. Saidi, M. Dammak, K. Soler-Carracedo and I. R. Martín, A Novel Optical Thermometry Strategy Based on Emission of  $\text{Tm}^{3+}/\text{Yb}^{3+}$  Codoped  $\text{Na}_3\text{GdV}_2\text{O}_8$  Phosphors, *Dalton Trans.*, 2022, 51(13), 5108–5117, DOI: [10.1039/D1DT03747A](https://doi.org/10.1039/D1DT03747A).
- 27 F. Ayachi, K. Saidi, M. Dammak, W. Chaabani, I. Mediavilla-Martínez and J. Jiménez, Dual-Mode Luminescence of  $\text{Er}^{3+}/\text{Yb}^{3+}$  Codoped  $\text{LnP}_{0.5}\text{V}_{0.5}\text{O}_4$  ( $\text{Ln} = \text{Y}, \text{Gd}, \text{La}$ ) for Highly Sensitive Optical Nanothermometry, *Mater. Today Chem.*, 2023, 27, 101352, DOI: [10.1016/j.mtchem.2022.101352](https://doi.org/10.1016/j.mtchem.2022.101352).
- 28 Nanomaterials|Free Full-Text|Bifunctional  $\text{Tm}^{3+}, \text{Yb}^{3+}:\text{GdVO}_4@ \text{SiO}_2$  Core-Shell Nanoparticles in HeLa Cells: Upconversion Luminescence Nanothermometry in the First Biological Window and Biolabelling in the Visible. <https://www.mdpi.com/2079-4991/10/5/993> (accessed 2023-09-30).
- 29 W. Zheng, H. Zhu, R. Li, D. Tu, Y. Liu, W. Luo and X. Chen, Visible-to-Infrared Quantum Cutting by Phonon-Assisted Energy Transfer in  $\text{YPO}_4:\text{Tm}^{3+}, \text{Yb}^{3+}$  Phosphors, *Phys. Chem. Chem. Phys.*, 2012, 14(19), 6974, DOI: [10.1039/c2cp24044k](https://doi.org/10.1039/c2cp24044k).
- 30 R. S. Yadav, S. J. Dhoble and S. B. Rai, Enhanced Photoluminescence in  $\text{Tm}^{3+}, \text{Yb}^{3+}, \text{Mg}^{2+}$  Tri-Doped  $\text{ZnWO}_4$  Phosphor: Three Photon Upconversion, Laser Induced Optical Heating and Temperature Sensing, *Sens. Actuators, B*, 2018, 273, 1425–1434, DOI: [10.1016/j.snb.2018.07.049](https://doi.org/10.1016/j.snb.2018.07.049).
- 31 V. Mahalingam, F. Vetrone, R. Naccache, A. Speghini and J. A. Capobianco, Colloidal  $\text{Tm}^{3+}/\text{Yb}^{3+}$ -Doped  $\text{LiYF}_4$  Nanocrystals: Multiple Luminescence Spanning the UV to NIR Regions via Low-Energy Excitation, *Adv. Mater.*, 2009, 21(40), 4025–4028, DOI: [10.1002/adma.200901174](https://doi.org/10.1002/adma.200901174).
- 32 M. Runowski, P. Woźny, N. Stopikowska, I. R. Martín, V. Lavín and S. Lis, Luminescent Nanothermometer Operating at Very High Temperature—Sensing up to 1000 K with Upconverting Nanoparticles ( $\text{Yb}^{3+}/\text{Tm}^{3+}$ ), *ACS Appl. Mater. Interfaces*, 2020, 12(39), 43933–43941, DOI: [10.1021/acsami.0c13011](https://doi.org/10.1021/acsami.0c13011).
- 33 T. Wang, Y. Li, T. Liu, Y. Peng, Z. Yin, Z. Yang, J. Qiu and Z. Song, NIR-NIR Upconverting Optical Temperature Sensing Based on the Thermally Coupled Levels of  $\text{Yb}^{3+}-\text{Tm}^{3+}$  Codoped  $\text{Bi}_7\text{F}_{11}\text{O}_5$  Nanosheets, *J. Lumin.*, 2020, 221, 117034, DOI: [10.1016/j.jlumin.2020.117034](https://doi.org/10.1016/j.jlumin.2020.117034).
- 34 I. Kachou, K. Saidi, U. Ekim, M. Dammak, M. Ç. Ersundu and A. E. Ersundu, Advanced Temperature Sensing with  $\text{Er}^{3+}/\text{Yb}^{3+}$  Co-Doped  $\text{Ba}_2\text{GdV}_3\text{O}_{11}$  Phosphors through Upconversion Luminescence, *Dalton Trans.*, 2024, 53(5), 2357–2372, DOI: [10.1039/D3DT04015A](https://doi.org/10.1039/D3DT04015A).
- 35 I. Kachou, M. Dammak, S. Auguste, F. Amiard and P. Daniel, A Novel Optical Temperature Sensor and Energy Transfer Properties Based on  $\text{Tb}^{3+}/\text{Sm}^{3+}$  Codoped  $\text{SrY}_2(\text{MoO}_4)_4$  Phosphors, *Dalton Trans.*, 2023, 52(48), 18233–18246, DOI: [10.1039/D3DT03410K](https://doi.org/10.1039/D3DT03410K).
- 36 K. Saidi, M. Dammak, K. Soler-Carracedo and I. R. Martín, A Novel Optical Thermometry Strategy Based on Emission of  $\text{Tm}^{3+}/\text{Yb}^{3+}$  Codoped  $\text{Na}_3\text{GdV}_2\text{O}_8$  Phosphors, *Dalton Trans.*, 2022, 51(13), 5108–5117, DOI: [10.1039/D1DT03747A](https://doi.org/10.1039/D1DT03747A).
- 37 C. D. S. Brites, A. Millán and L. D. Carlos, Lanthanides in Luminescent Thermometry. *Handbook on the Physics and Chemistry of Rare Earths*, Elsevier, 2016, vol. 49, pp. 339–427, DOI: [10.1016/bs.hpcr.2016.03.005](https://doi.org/10.1016/bs.hpcr.2016.03.005).
- 38 K. Saidi, I. Kachou, K. Soler-Carracedo, M. Dammak and I. R. Martín,  $\text{Ba}_2\text{YV}_3\text{O}_{11} \text{Er}^{3+}/\text{Yb}^{3+}$  Nanostructures for Temperature Sensing in the Presence of Bismuth Ions, *ACS Appl. Nano Mater.*, 2023, 6(19), 17681–17690, DOI: [10.1021/acsanm.3c02911](https://doi.org/10.1021/acsanm.3c02911).
- 39 M. Huang, M. Dai, K. Li, Y. Wei and Z. Fu, Engineering Dual-Mode near-Infrared Ratiometric Thermometers Based on Rare Earth-Doped Molybdates, *Spectrochim. Acta, Part A*, 2025, 329, 125603, DOI: [10.1016/j.saa.2024.125603](https://doi.org/10.1016/j.saa.2024.125603).
- 40 K. Saidi, M. Yangui, C. Hernández-Álvarez, M. Dammak, I. Rafael Martín Benenzuela and M. Runowski, Multifunctional Optical Sensing with Lanthanide-Doped Upconverting Nanomaterials: Improving Detection Performance of Temperature and Pressure in the Visible and NIR Ranges, *ACS Appl. Mater. Interfaces*, 2024, 16(15), 19137–19149, DOI: [10.1021/acsami.4c00313](https://doi.org/10.1021/acsami.4c00313).
- 41 Z. E. A. A. Taleb, K. Saidi and M. Dammak, High-Precision Optical Thermometry Using  $\text{Pr}^{3+}$ -Doped  $\text{NaCaY}(\text{MoO}_4)_3$  Luminophores: A Multi-Spectral and Chromaticity-Based Approach to Non-Contact Temperature Sensing, *RSC Adv.*, 2025, 15(7), 5327–5337, DOI: [10.1039/D5RA00093A](https://doi.org/10.1039/D5RA00093A).
- 42 N. B. Amar, K. Saidi, C. Hernández-Álvarez, M. Dammak and I. R. Martín, Ultra-High-Sensitive Temperature Sensing Based on Emission  $\text{Pr}^{3+}$  and  $\text{Yb}^{3+}$  Codoped  $\text{Y}_2\text{Mo}_3\text{O}_{12}$  Nanostructures, *Mater. Adv.*, 2025, 6(2), 827–838, DOI: [10.1039/D4MA00746H](https://doi.org/10.1039/D4MA00746H).
- 43 S. Chen, W. Song, J. Cao, F. Hu and H. Guo, Highly Sensitive Optical Thermometer Based on FIR Technique of Transparent  $\text{NaY}_2\text{F}_7:\text{Tm}^{3+}/\text{Yb}^{3+}$  Glass Ceramic, *J. Alloys Compd.*, 2020, 825, 154011, DOI: [10.1016/j.jallcom.2020.154011](https://doi.org/10.1016/j.jallcom.2020.154011).
- 44 M. Runowski, A. Shyichuk, A. Tymiąski, T. Grzyb, V. Lavín and S. Lis, Multifunctional Optical Sensors for Nanomanometry and Nanothermometry: High-Pressure and High-Temperature Upconversion Luminescence of Lanthanide-Doped Phosphates— $\text{LaPO}_4/\text{YPO}_4:\text{Yb}^{3+}-\text{Tm}^{3+}$ , *ACS Appl. Mater. Interfaces*, 2018, 10(20), 17269–17279, DOI: [10.1021/acsami.8b02853](https://doi.org/10.1021/acsami.8b02853).
- 45 O. A. Savchuk, J. J. Carvajal, J. Massons, C. Cascales, M. Aguiló and F. Díaz, Novel Low-Cost, Compact and Fast Signal Processing Sensor for Ratiometric Luminescent Nanothermometry, *Sens. Actuators, A*, 2016, 250, 87–95, DOI: [10.1016/j.sna.2016.08.031](https://doi.org/10.1016/j.sna.2016.08.031).



- 46 U. Rocha, K. U. Kumar, C. Jacinto, I. Villa, F. Sanz-Rodríguez, M. del Carmen Iglesias de la Cruz, A. Juarranz, E. Carrasco, F. C. J. M. van Veggel, E. Bovero, J. G. Solé and D. Jaque, Neodymium-Doped LaF<sub>3</sub> Nanoparticles for Fluorescence Bioimaging in the Second Biological Window, *Small*, 2014, **10**(6), 1141–1154, DOI: [10.1002/smll.201301716](https://doi.org/10.1002/smll.201301716).
- 47 U. Rocha, C. Jacinto da Silva, W. Ferreira Silva, I. Guedes, A. Benayas, L. Martínez Maestro, M. Acosta Elias, E. Bovero, F. C. J. M. van Veggel, J. A. García Solé and D. Jaque, Subtissue Thermal Sensing Based on Neodymium-Doped LaF<sub>3</sub> Nanoparticles, *ACS Nano*, 2013, **7**(2), 1188–1199, DOI: [10.1021/nn304373q](https://doi.org/10.1021/nn304373q).

